Effects of a nonadiabatic wall on hypersonic shock/boundary-layer interactions

Pedro S. Volpiani,[1] Matteo Bernardini,[2] and Johan Larsson[1]
[1]*Department of Mechanical Engineering, University of Maryland, College Park, Maryland 20742, USA*
[2]*Dipartimento di Ingegneria Meccanica e Aerospaziale, Università di Roma "La Sapienza", Via Eudossiana 18, 00184 Rome, Italy*

(Received 27 July 2019; published 21 January 2020)

High-fidelity numerical simulations of an impinging shock interacting with a turbulent boundary layer at free-stream Mach number $\mathrm{Ma}_\infty = 5.0$ are performed for three shock angles and a weakly cooled wall condition (wall-to-recovery temperature ratio of $T_w/T_r = 0.8$), matching the experimental conditions of Schülein [AIAA J. **44**, 1732 (2006)]. Additional simulations are carried out with a heated wall ($T_w/T_r = 1.9$) to investigate the impact of the wall thermal condition on shock/boundary-layer interactions in the hypersonic regime. The free interaction theory is found to remain valid in the hypersonic regime even at different wall thermal conditions. The interaction length scaling proposed by Jaunet *et al.* [AIAA J. **52**, 2524 (2014)] previously validated only at supersonic Mach numbers, is found to remain viable at higher Mach numbers only if the model coefficient is adjusted, thus showing that this coefficient is not universal.

DOI: 10.1103/PhysRevFluids.5.014602

I. INTRODUCTION

Air frames and air breathing propulsion systems of hypersonic vehicles are often exposed to large aerothermodynamic loads related to a complex interaction between shock waves and turbulent boundary layers (referred to as SBLI in the following). This phenomenon has most of the time a negative impact on the aerodynamic performance of the vehicle, through its influence on the global force coefficients. For example, the flow over an activated control surface creates an oblique shock which, for a sufficiently large deflection angle, will cause the boundary layer to separate due to the local adverse pressure gradient. The flow separation resulting from the interaction can induce instabilities, reducing the performance of the control surface and can generate significant thermal loads, all of which are critical for vehicle design. The accurate prediction of the aerodynamic heating in a hypersonic flight is an important step in the design process, which can reduce the weight of the vehicle, increase the payload, and enhance the fuel efficiency.

The majority of the work on supersonic shock/boundary-layer interactions [1–14] has kept the wall temperature fixed, most of time at the adiabatic condition, and has not systematically analyzed the effect of the wall heat flux on the interaction. Only a few experiments have systematically studied the effect of the wall thermal condition on the SBLI flow field specifically [15–17]. Jaunet *et al.* [17] investigated experimentally the impact of changing the wall temperature on a $\mathrm{Ma}_\infty = 2.3$ shock-induced boundary-layer separation. They varied the shock deflection angle from 3.5° to 9.5° and the wall-to-recovery-temperature ratio from $T_w/T_r = 1$ (adiabatic) to $T_w/T_r = 1.9$ (heated condition). Three main conclusions emerged from their analysis: (i) the interaction length significantly increases when the wall temperature is elevated, due to changes in the incoming boundary layer; (ii) the onset of separation is shifted to smaller shock strengths in the heated case; and (iii) the lower frequencies of the flow unsteadiness become more important by heating the wall. On the numerical side, only recently the effect of the wall thermal condition for turbulent SBLI was investigated by means of direct numerical simulations (DNS) [18,19]. Bernardini *et al.* [18] performed simulations of SBLI at $\mathrm{Ma}_\infty = 2.3$ at different wall conditions. Volpiani *et al.* [19] extended the database and included several deflection angles. The numerical results indicate that wall cooling minimizes the flow separation but increases the wall pressure fluctuations. It was shown that the changes in the interaction length due to the wall thermal condition are mainly linked to the incoming boundary layer, which is in agreement with previous experimental studies.

As discussed by Settles and Dodson [20], the experimental database for turbulence at Mach numbers greater than 5 is extremely limited, especially when the focus is the effect of the surface temperature on the hypersonic SBLI. Elfstrom [21] and Holden [22] performed experiments at free-stream Mach numbers up to 9.22 and 13, respectively, with different cooled wall conditions. Their studies indicate that cooling increases the boundary layer resistance to separation at hypersonic speeds. Schülein and co-workers [23,24] used nonintrusive techniques to measure the skin-friction coefficient and the heat transfer rate in a SBLI of an impinging shock at $\mathrm{Ma}_\infty = 5$ and wall-to-recovery temperature ratio of $T_w/T_r = 0.8$. They found a strong increase of the heat flux in the separation zone. Surface heat transfer was also assessed by Sandham *et al.* [25] in a transitional SBLI at $\mathrm{Ma}_\infty = 6$, allowing the peak Stanton number in the reattachment regime to be mapped over a range of intermittency states of the approaching boundary layer. They showed that the highest levels of wall heat transfer were consistently obtained for transitional rather than fully turbulent interactions. Wagner *et al.* [26] investigated a $\mathrm{Ma}_\infty = 7.4$ SBLI at a compression corner and focused on the effect of the leading-edge bluntness and the surface temperature. They confirmed that the state of the incoming boundary layer plays an important role in the characteristics of the interaction, in agreement with other studies carried out in the supersonic regime [17,19,27]. They showed that a small change of the leading-edge bluntness or in the surface heating affected the boundary-layer stability and consequently the SBLI. Despite the promising results, a well-defined boundary-layer state was not fully determined, making it difficult to reproduce this experiment numerically.

This paper is an extension of our previous work [19] that investigated the effects of nonadiabatic walls on supersonic shock/turbulent-boundary-layer interactions using direct numerical simulations. The objectives of this study are to (i) analyze the impact of the wall thermal condition and deflection angles on SBLI in the hypersonic regime by means of high-fidelity numerical simulations, and (ii) compare our numerical data with the experiment performed by Schülein [23] at free-stream Mach number $\mathrm{Ma}_\infty = 5$.

II. NUMERICAL APPROACH

The three-dimensional compressible Navier-Stokes equations for an ideal gas are solved in conservative form in a Cartesian coordinate frame as

$$\partial_t \mathbf{Q} + \partial_j \mathbf{F}_i - \partial_j \mathbf{F}_v = 0.$$

The state vector $\mathbf{Q} = [\rho, \rho u_i, \rho E]^T$ consists of density ρ, momentum ρu_i, and total energy $\rho E = p/(\gamma - 1) + \rho u_i^2/2$, where p is the pressure and u_i the velocity component in direction i. The ratio of specific heats is constant $\gamma = 1.4$. The inviscid and viscous fluxes are, respectively,

$$\mathbf{F}_i = [\rho u_j, \rho u_i u_j + p\delta_{ij}, (\rho E + p)u_j]^T,$$
$$\mathbf{F}_v = [0, \tau_{ij}, u_i\tau_{ij} + q_j]^T.$$

The fluid is assumed to be Newtonian and according to the Stokes hypothesis, the viscous stress tensor is given by

$$\tau_{ij} = \mu\left(\frac{\partial u_i}{\partial x_j} + \frac{\partial u_j}{\partial x_i} - \frac{2}{3}\frac{\partial u_k}{\partial x_k}\delta_{ij}\right).$$

The heat flux is modeled by Fourier's law as

$$q_j = -\frac{C_p \mu}{\mathrm{Pr}} \partial_j T.$$

The viscosity is assumed to follow the power law $\mu = \mu_{\mathrm{ref}}(T/T_{\mathrm{ref}})^{3/4}$, and the Prandtl number is taken as $\mathrm{Pr} = 0.7$.

The system of equations are nondimensionalized by the free-stream values of velocity, temperature, and density and the boundary-layer thickness. The fluid is assumed to behave as an ideal gas with equation of state $p = R\rho T$, where the nondimensional gas constant is $R = 1/(\gamma \mathrm{Ma}_\infty^2)$. The specific heat is $C_p = \gamma R/(\gamma - 1)$.

The governing equations are solved using an in-house finite difference code based on a solution-adaptive numerical scheme. Near shocks, a fifth-order accurate weighted essentially nonoscillatory (WENO) scheme with Roe flux splitting is used to approximate the inviscid fluxes, whereas a sixth-order accurate central difference scheme in the split form by Ducros *et al.* [28] is used in the remainder of the domain. The sensor $s = -\xi/(|\xi| + \langle \omega_j \omega_j \rangle^{1/2})$ is used to identify regions of shock waves at every time step, where $\xi = \partial_j u_j$ is the dilatation, $\omega_i = \epsilon_{ijk} \partial_j u_k$ is the vorticity, and $\langle \cdot \rangle$ is a local average. The WENO scheme is applied in regions where $s > 0.7$. The viscous terms are treated by a conservative scheme that has the resolution characteristics of a sixth-order scheme, and the system is integrated in time using a fourth-order accurate Runge-Kutta method. The code has been thoroughly verified on several benchmark problems [29].

The inflow turbulence is generated using the digital filtering technique by Klein *et al.* [30] and Touber and Sandham [10], which has been proven to not introduce any significant low frequencies into the domain. This technique was validated in a previous study [19] and is employed herein. In this study, filtering length scales of 0.6 and 0.2 δ_{in} are used in the streamwise and spanwise directions. The length scale in the wall-normal direction is taken as 0.04 δ_{in} near the wall and 0.2 δ_{in} in the free stream, with a smooth transition in-between. The mean velocity and Reynolds stress profiles are taken from incompressible databases [31,32]. The mean temperature and density are assumed to follow Walz's relation, and the fluctuating quantities are assumed to follow the strong Reynolds analogy (cf. [33]). The shock is artificially generated at the top boundary by enforcing the inviscid oblique shock solution corresponding to each flow deflection angle and the flow field is then let to evolve until it reaches a statistically steady state. It is noteworthy mentioning that for the 14° wedge cases, the transient time is quite long (around $400\delta_{\mathrm{in}}/u_\infty$), compared to $150\delta_{\mathrm{in}}/u_\infty$ for the other cases. Periodicity is imposed in the spanwise direction.

The computational domain for all cases has an overall extent $L_x \times L_y \times L_z = 70\delta_{\mathrm{in}} \times 10\delta_{\mathrm{in}} \times 5\delta_{\mathrm{in}}$, where δ_{in} is the boundary-layer thickness at the inlet. Grid nodes are uniformly distributed in the streamwise (x) and spanwise (z) directions. For the wall-normal direction (y) a stretching function based on a hyperbolic cosine mapping is used, in order to gather points closer to the wall.

The ensemble averages of the flow variables were obtained by considering a total of 200 samples of the flow field for the boundary layer and 300 samples for the SBLI cases, taken at constant time intervals $\Delta t = \delta_{\mathrm{in}}/u_\infty$ and averaging in the spanwise direction.

III. MACH 5 EXPERIMENT OVERVIEW

Schülein and co-workers [23,24] conducted a Mach 5 impinging SBLI experiment in the DLR Göttingen wind tunnel. The nominal free-stream conditions are shown in Table I. The measured quantities included wall pressure, skin friction, and wall heat transfer. Skin friction was measured by an oil-flow technique and computed indirectly by the log-law from probe measurements. Wall heat transfer was measured by infrared thermography technique. The quoted experimental uncertainties are approximately 2% for pressures, 10% for skin friction, and 20% for heat flux. The total enthalpy was sufficiently low to make high-temperature effects, including dissociation, negligible. The upstream boundary layer was fully developed and the oblique shock impinged the flat plate at $x_{\mathrm{imp}} = 350$ mm from the leading edge. Four configurations were tested, starting from

TABLE I. Nominal test conditions for Schülein's experiment. Ma_∞: Mach number, P_0: stagnation pressure, $H_{0,\infty}$: stagnation enthalpy, T_0: stagnation temperature, T_w: wall temperature, Re_m: Reynolds number per meter, U_∞: free-stream velocity, ρ_∞: free-stream density, T_w/T_r: wall-to-recovery temperature ratio.

Ma_∞	P_0	$H_{0,\infty}$	T_0	T_w	Re_m	U_∞	ρ_∞	T_w/T_r
5.0	2.2 MPa	0.41 MJ/kg	410 K	300 K	37×10^6 m^{-1}	825 m/s	0.2159 kg/m^3	0.8

a two-dimensional (2D) nominal zero-pressure gradient flat plate boundary layer and with three different shock generator angles β of 6°, 10°, and 14°. These flow deflection angles produced attached, incipient, and separated SBLI cases, respectively.

IV. BOUNDARY-LAYER SIMULATIONS

Simulations without the impinging shock are carried out to validate the inflow condition and assess the state of the turbulent boundary layer. Two wall-to-recovery-temperature ratios are considered in this study: a weakly cooled wall with $T_w/T_r = 0.8$ (as in the experiment), and an additional heated wall $T_w/T_r = 1.9$. This latter condition was chosen to be in the realistic range since recent experiments carried out in the same facility achieved wall temperatures up to $T_w = 800$ K. The recovery temperature T_r is computed as (cf. [33])

$$\frac{T_r}{T_\infty} = 1 + r\frac{\gamma - 1}{2}\mathrm{Ma}_\infty^2 , \tag{1}$$

where the subscript ∞ denotes conditions at the edge of the boundary layer (local free-stream), so that the edge Mach number $\mathrm{Ma}_\infty = U_\infty/\sqrt{\gamma R T_\infty}$. The recovery factor is taken as $r = \mathrm{Pr}^{1/3}$.

Details of the mesh are given in Table II. Note that wall cooling leads to a drastic reduction in the viscous length scale, which leads to much more demanding grid requirements for the cold wall case. Note also that the strictest grid requirements for the heated case come from the outer part of the boundary layer, leading to this case having an excessively fine grid spacing in viscous units near the wall.

In order to compare simulations at different wall conditions, Volpiani *et al.* [19] matched the Reynolds number $\mathrm{Re}_\tau^* = \rho_\infty(\tau_w/\rho_\infty)^{1/2}\delta/\mu_\infty$, following the work by Trettel and Larsson [34]. Since it is not known which specific Reynolds number best describes high-speed wall-bounded flows across different conditions (Mach, T_w/T_r, shock strength, etc.), the decision in this study was to compute both T_w/T_r cases at fixed $\mathrm{Re}_\theta \approx 3800$, and then to consider an additional case BL-0.8-5400 at a higher Reynolds number ($\mathrm{Re}_\theta \approx 5400$) which matches the same Re_τ^* as in the heated case. The Reynolds numbers at the shock impinging location ($x_{\mathrm{imp}} = 40\delta_{\mathrm{in}}$) are listed in Table III together with the estimated experimental values.

Figure 1(a) shows the Van Driest transformed mean velocity profile at station $x_{\mathrm{imp}} = 40\delta_{\mathrm{in}}$ for simulations having weakly cooled walls (BL-0.8-3800 and BL-0.8-5400). The density-scaled

TABLE II. Mesh configuration for the DNS of hypersonic boundary layers. The table presents the wall-to-recovery-temperature ratio T_w/T_r, the number of points, and the grid spacing in terms of wall units in each direction.

Simulation	T_w/T_r	N_x	N_y	N_z	Δx^+	Δy_w^+	Δz^+
BL-1.9-3800	1.9	1600	340	140	4.4	0.7	3.8
BL-0.8-3800	0.8	2400	400	200	6.7	1.	5.9
BL-0.8-5400	0.8	2400	440	300	9.7	1.	5.7
BL-0.8-7000	0.8	2600	460	340	11.5	1.	6.5

TABLE III. Global characteristics of the turbulent boundary layers at $x_{\mathrm{imp}} = 40\delta_{\mathrm{in}}$. The Reynolds numbers are defined as $\mathrm{Re}_\delta = \rho_\infty u_\infty \delta/\mu_\infty$, $\mathrm{Re}_\theta = \rho_\infty u_\infty \theta/\mu_\infty$, $\mathrm{Re}_{\delta_2} = \rho_\infty u_\infty \theta/\mu_w$, $\mathrm{Re}_\tau = \rho_w u_\tau \delta/\mu_w$, and $\mathrm{Re}_\tau^* = \rho_\infty(\tau_w/\rho_\infty)^{1/2}\delta/\mu_\infty$, where θ is the momentum thickness and u_τ the friction velocity. The experimental values were estimated at station 356 mm.

Simulation	Re_δ	Re_θ	Re_{δ_2}	Re_τ	Re_τ^*
BL-1.9-3800	138000	3890	675	175	3150
BL-0.8-3800	90800	3764	1250	390	2390
BL-0.8-5400	134000	5415	1800	552	3395
BL-0.8-7000	173000	6940	2300	687	4235
Expt. [23,24]	180000	7400	1900		

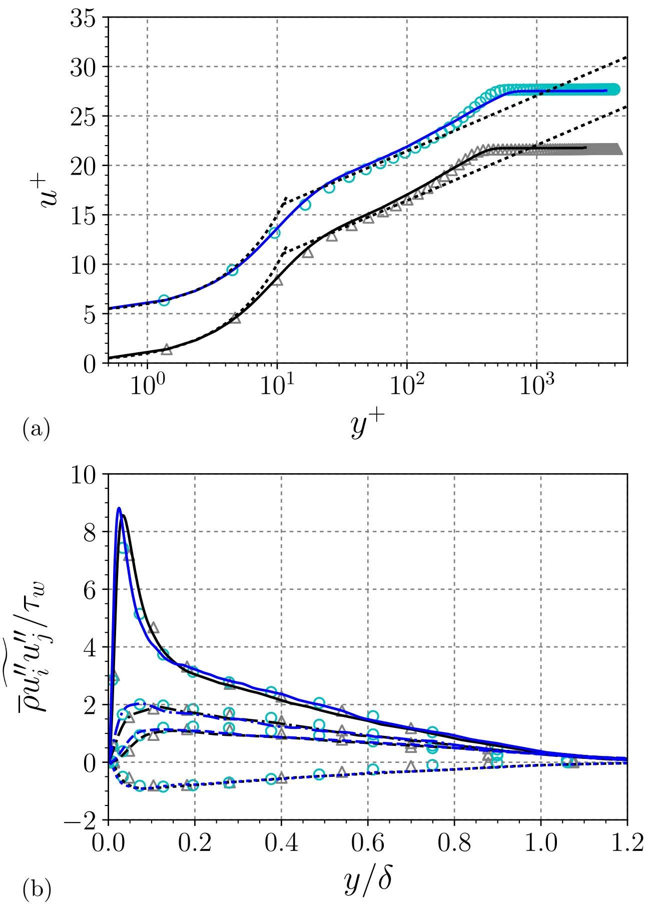

FIG. 1. Comparison of boundary layers BL-0.8-3800 and BL-0.8-5400 at station $x_{\mathrm{imp}} = 40\delta_{\mathrm{in}}$ (lines) with the incompressible DNS results of Schlatter and Örlü [35] at $\mathrm{Re}_\tau = 359$ (triangles) and $\mathrm{Re}_\tau = 492$ (circles). (a) Van Driest transformed mean velocity profile (solid line). Simulation BL-0.8-5400 is shifted vertically. The linear $u^+ = y^+$ and log-law $u^+ = 5.2 + 2.44 \ln y^+$ are also represented (dotted lines). (b) Density-scaled Reynolds stress components: longitudinal (solid line), wall-normal (dashed line), transverse (dotted-dashed line), and shear stress (dotted line).

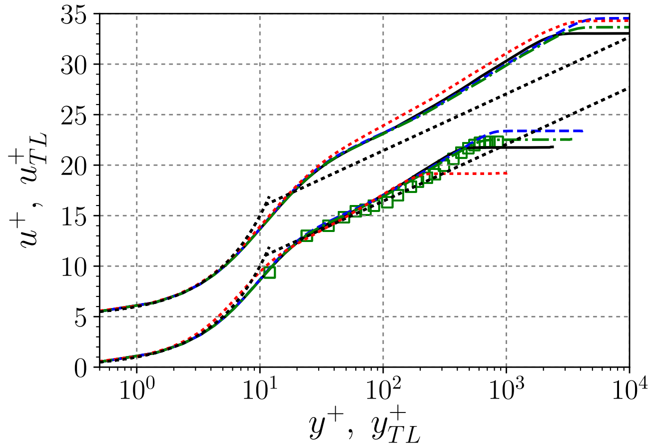

FIG. 2. Assessment of the boundary layer at station $x_{\text{imp}} = 40\delta_{\text{in}}$. Van Driest transformed mean velocity u^+ plotted vs $y^+ = y\sqrt{\rho_w \tau_w}/\mu_w$ compared to the experiments of Schülein [23] (symbols). The vertically offset lines are the velocity transformed according to Trettel and Larsson [34] (u^+_{TL}) plotted vs the semilocally scaled y^+_{TL}. Cases BL-0.8-3800 (solid line), BL-1.9-3800 (dotted line), BL-0.8-5400 (dashed-dotted line), and BL-0.8-7000 (dashed line).

Reynolds stresses are shown in Fig. 1(b). The incompressible DNS results of Schlatter and Örlü [35] at similar Reynolds numbers, both (i) $\text{Re}_\theta = \text{Re}_{\delta_2} = 1006$ and $\text{Re}_\tau = 359$ and (ii) $\text{Re}_\theta = \text{Re}_{\delta_2} = 1421$ and $\text{Re}_\tau = 492$ are also shown in Fig. 1 and are in close agreement with the present mean velocity and root mean square (rms) profiles. Note that the peak of the longitudinal stress occurs at the same location as in the adiabatic data, but with a higher value due to the fact that the wall is weakly cooled [19]. This comparison validates our numerical method and proves that the inflow boundary condition and the development length of $40\delta_{\text{in}}$ are sufficient to produce realistic turbulence. For reference, $\delta_{\text{imp}}/\delta_{\text{in}} \approx 1.6$ with slight variations among the different cases.

Figure 2 shows the mean velocity profiles from all cases together with the experimental data from Schülein [23,24]. Curiously, the experimental results do not match with the simulation at the highest Reynolds number and are instead closer to the intermediate BL-0.8-5400 case in the outer layer. For this reason, the SBLI simulation corresponding to the boundary layer BL-0.8-7000 was not performed.

In the same figure, results using the more recent transformation by Trettel and Larsson [34] are also included, for which

$$y^+_{\text{TL}} = \frac{y\overline{\rho}}{\overline{\mu}}\sqrt{\frac{\tau_w}{\overline{\rho}}}, \tag{2a}$$

$$\begin{aligned} u^+_{\text{TL}} &= \int_0^{u^+} \left(\frac{\overline{\rho}}{\rho_w}\right)^{1/2} \left[1 + \frac{1}{2}\frac{1}{\overline{\rho}}\frac{d\overline{\rho}}{dy}y - \frac{1}{\overline{\mu}}\frac{d\overline{\mu}}{dy}y\right] du^+ \\ &= \int_0^{u^+} \left(\frac{\overline{\mu}}{\mu_w}\right) \frac{dy^+_{\text{TL}}}{dy^+} du^+. \end{aligned} \tag{2b}$$

Note that this transformation affects both the velocity and the wall-normal coordinate, i.e., u^+_{TL} must be plotted vs y^+_{TL}. This “coupling” between the velocity and the coordinate is explicit in the second form of the velocity transformation (2b). Also note that y^+_{TL} is more commonly referred to as the semilocal scaling y^*.

While the Van Driest transformation is known to be accurate for adiabatic surfaces, the second transformation was developed for flows with significant wall heating/cooling. The results in Fig. 2

TABLE IV. Flow parameters for the SBLI simulations at free-stream Mach number $\mathrm{Ma}_\infty = 5$. T_w/T_r: wall-to-recovery-temperature ratio, φ is the incidence angle of the shock generator. H stands for the simulation performed at higher Reynolds number.

Simulation	T_w/T_r	φ (deg)	T_w/T_∞	Grid points
SBLI-0.8-06	0.8	6.0°	4.36	192 M
SBLI-0.8-10	0.8	10.0°	4.36	192 M
SBLI-0.8-14	0.8	14.0°	4.36	192 M
SBLI-0.8-14-H	0.8	14.0°	4.36	317 M
SBLI-1.9-06	1.9	6.0°	10.36	76 M
SBLI-1.9-10	1.9	10.0°	10.36	76 M
SBLI-1.9-14	1.9	14.0°	10.36	76 M

show that the newer transformation in Eq. (2) better captures the thickness of the viscous buffer layer. However, we also note that this transformation produces an upward shift in the log-layer, which stands in contrast to the results on channel flows in Trettel and Larsson [34]. These results suggest that the newer transformation needs a correction at higher Mach numbers, especially at the heated condition. This issue is discussed in a separate paper [36].

V. SBLI SIMULATIONS

In this section, the effects of the deviation angle and the wall temperature on the $\mathrm{Ma}_\infty = 5$ SBLI flow field are analyzed. This is followed by solution verification, primarily an assessment of the effect of the computational grid. Finally, the pressure spectra and similarity scaling are discussed.

The same grid used to run the previous boundary-layer cases is employed in the SBLI simulations. The shock impingement point is set at $x_{\mathrm{imp}} = 40\delta_{\mathrm{in}}$ for all cases. In the following, the origin is placed at x_{imp}, and lengths are made nondimensional with respect to the boundary-layer thickness δ_{imp} at the nondisturbed reference station $x_{\mathrm{imp}} = 40\delta_{\mathrm{in}}$. Thus, the nondimensional interaction coordinates are written as $(x - x_{\mathrm{imp}})/\delta_{\mathrm{imp}}$ and y/δ_{imp}. All SBLI simulations are summarized in Table IV.

A. Effect of deflection angle and comparison with experiments

As described by Délery and Dussauge [37], there are two shock waves in a weak SBLI: the impinging shock and the reflected shock formed by the compression waves coming from the front and rear portion of the expanded boundary-layer subsonic region. In this case, the pressure rises smoothly through the interaction region attaining the inviscid pressure jump. In a strong interaction, on the other hand, the boundary layer detaches and the mean pressure profile through the interaction region exhibits a plateau in the separation zone. At the leading edge of the separation bubble, compression waves form the reflected shock. The flow deflection at the top of the bubble generates an expansion fan followed by compression waves that may or may not gather with the compression wave generated at the leading edge of the separation bubble (see Figs. 3 and 4).

Here, we study configurations characteristic of weak, incipient, and strong interactions. Differently from supersonic SBLI studies, the strong interaction ($\varphi = 14°$) presents two strong reflected waves as illustrated in Fig. 3, which shows the three-dimensional field of the Q-criterion isosurface colored by the streamwise velocity and dilatation isosurface to illustrate incident and reflecting shocks. This 3D visualization highlights the turbulent structures of the boundary layer and the complex waves that are originated by the interaction.

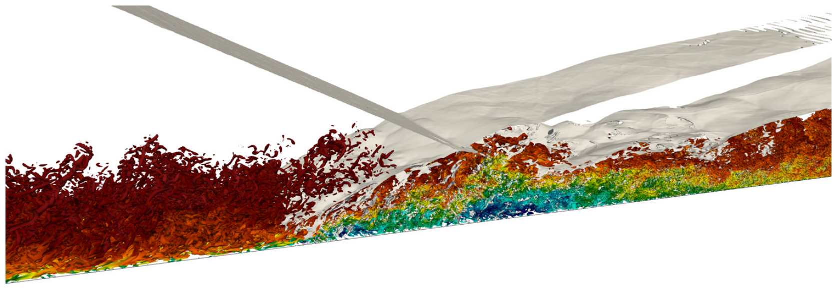

FIG. 3. Isosurface of the Q criterion colored by the streamwise velocity and dilatation isosurface (gray) for the simulation SBLI-0.8-14: $T_w/T_r = 0.8$ and $\varphi = 14^\circ$.

We report in Fig. 4 the instantaneous and mean streamwise velocity fields in the *xy* plane for cases with $\varphi = 6^\circ$, 10°, and 14°. It is clear that the size of the recirculation bubble increases when φ increases.

Simulations with $T_w/T_r = 0.8$ are now analyzed and compared with experimental data. The average skin friction coefficient $C_f = 2\tau_w/\rho_\infty u_\infty^2$ is displayed in Fig. 5(a) for the three deflection angles considered. The friction coefficient is qualitatively different from the $\mathrm{Ma}_\infty = 2.3$ results of Volpiani *et al.* [19], where C_f became distinctly negative immediately at separation; in the present $\mathrm{Ma}_\infty = 5$ results, C_f instead becomes only slightly negative at first, followed by a later dip.

The experiments by Schülein [23] have qualitatively similar C_f profiles (a weakly negative region followed by a more pronounced dip) but with much earlier separation: the boundary layer separates about 2 δ_{imp} earlier for $\varphi = 14^\circ$ and about 1 δ_{imp} earlier for $\varphi = 10^\circ$. For the $\varphi = 6^\circ$ case, the experiment (data not shown in the figure) indicates attached flow without any separation while the simulation has a very small separated region.

The reason for this disagreement is not known. One possible explanation is the boundary layer on the wedge that creates the impinging shock, which would increase the shock strength and also cause

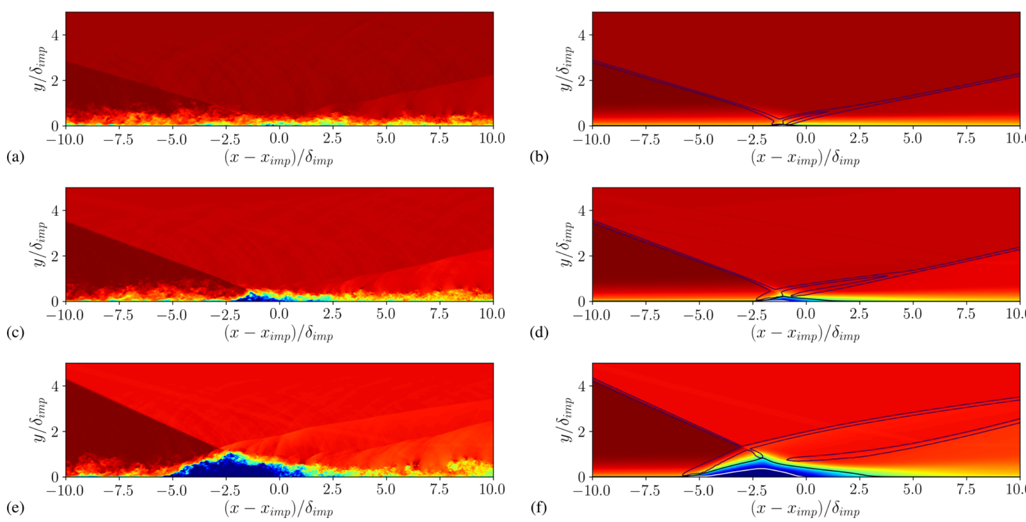

FIG. 4. Instantaneous (left) and mean (right) streamwise velocity field $\overline{u}$ at various incidence angle of the shock generator and $T_w/T_r = 0.8$: $\varphi = 6^\circ$ (a), (b), $\varphi = 10^\circ$ (c), (d) and $\varphi = 14^\circ$ (e), (f). Contour levels are shown in the range $0 < \overline{u}/u_\infty < 1$. The white line denotes the zero level and the black one the sonic line. Isocontour of the mean dilatation is also shown in dark purple.

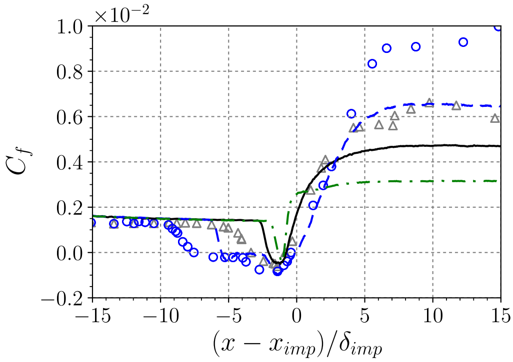

(a)Distribution of the mean skin friction coefficient

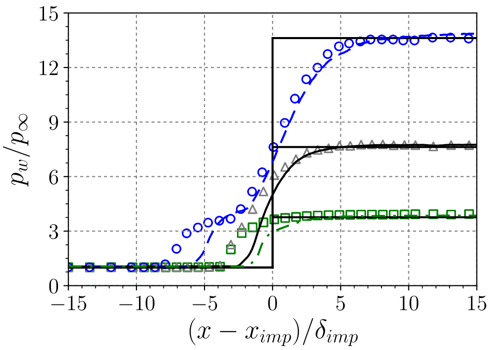

(b)Distribution of the mean wall pressure

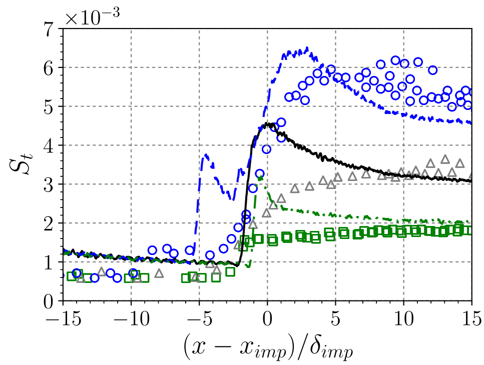

(c)Distribution of the mean Stanton number

FIG. 5. Mean flow properties across the interaction zone at various deflection angles and $T_w/T_r = 0.8$: case SBLI-0.8-14 (dashed line), SBLI-0.8-10 (solid line), and SBLI-0.8-06 (dashed-dotted line). Symbols indicate experimental data from Schülein [23]. (a) Distribution of the mean skin friction coefficient. (b) Distribution of the mean wall pressure. (c) Distribution of the mean Stanton number.

an upstream shift of the shock impingement location. However, this hypothesis is rejected here since the mean pressure jumps agree very well between the experiment and the simulation [Fig. 5(b)]. Another hypothesis is that the disagreement is a Reynolds number effect. However, the difference between the high and nominal Reynolds number cases in Fig. 7 is very small, and we therefore reject this hypothesis as well. The next possibility is that the disagreement stems from differences in the incoming boundary layer. The skin friction coefficient C_f is slightly smaller in the experiment than in the simulation, but the Stanton number is smaller by almost a factor of 2 in the experiment. The temperature in the simulation closely follows the Walz relation (not shown) and is fully developed at the shock impingement location. The simulation does not have an entropy layer since we do not include the leading edge in the computation, but this difference should cause a larger wall heat flux in the experiment, opposite of what is observed; in addition, the experiment was conducted with a very sharp leading edge which should not cause a large entropy layer. The last hypothesis is that the discrepancy is caused by three-dimensional (3D) effects, i.e., by the finite span of the plate in the experiment. Bruce *et al.* [38] studied the effect of confinement from tunnel walls (and the associated corner flows) on planar SBLI, and found that the effect could be parametrized by the ratio of the displacement thickness δ^* to the width of the test section. In very approximate terms, they found the effect of confinement to be significant for $\delta^*/L_z \gtrsim 0.002$–$0.004$. The equivalent parameter for the experiment by Schülein [23] is $\delta^*/L_z \approx 0.005$. While the confinement characteristics of the

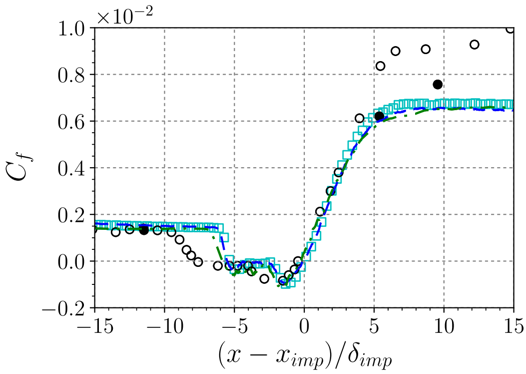

(a)Distribution of the mean skin friction coefficient

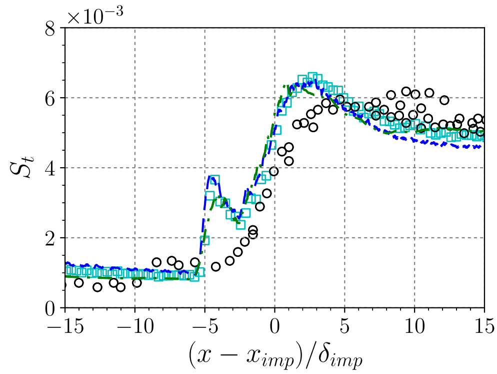

(b)Distribution of the mean Stanton number

FIG. 6. Mean flow properties across the interaction zone at $T_w/T_r = 0.8$ and deflection angle $\varphi = 14^\circ$: base grid (dashed line), fine grid (squares), and fine grid using Rome's code (dashed-dotted line). Circles indicate experimental measurements from Schülein [23]. In (a), the open circles are from oil film interferometry while the closed circles are from the measured velocity profile. (a) Distribution of the mean skin friction coefficient. (b) Distribution of the mean Stanton number.

latter is entirely different (a flat plate without sides immersed in a free stream), it nevertheless seems plausible that the experiment has significant 3D effects. Of particular note is that Bruce *et al.* [38] found a rather strong effect on the size and location of the separation bubble. To conclude, while the reason for the discrepancy between the simulation and the experiment is not known at this point, the most plausible explanation is that the discrepancy is caused by 3D effects, specifically related to the effect of the finite width of the flat plate in the experiment. We note that inclusion of the full width of the plate would increase the computational cost by at the very least a factor of 30.

The mean wall pressure normalized by the free-stream pressure is shown in Fig. 5(b). The pressure jump predicted by the inviscid theory is well recovered in both cases. As discussed in Volpiani *et al.* [19], the mean wall pressure distribution is typical of a weak interaction for $\varphi = 6^\circ$ and 10° and typical of strong interaction for $\varphi = 14^\circ$. In the first case, the pressure rise is smooth, while in the latter, a pressure plateau is observed.

The heat transfer rate can be characterized by the spatial distribution of the Stanton number

$$\mathrm{St} = \frac{q_w}{\rho_\infty u_\infty C_p (T_w - T_r)}, \qquad q_w = -k \frac{d\overline{T}}{dy}\bigg|_w \tag{3}$$

which is plotted in Fig. 5(c). Note that Schülein [23] used the stagnation temperature T_0 instead of the recovery temperature T_r in the definition of the Stanton number; this was rescaled to use T_r in all plots here. A strong amplification of the heat transfer rate is found in the interaction region with respect to the reference boundary layer and is higher for large shock strengths. For case $\varphi = 14^\circ$, the heat transfer rate is around seven times higher than the reference boundary-layer case before the interaction. The Stanton number distribution has a minimum at the mean separation point and increases nonmonotonically for strong interactions (see also Hayashi *et al.* [14]).

B. Solution verification

The adequacy of the synthetic inflow turbulence and the chosen inflow development length to produce realistic fully developed turbulence was assessed above for the boundary-layer simulations. The focus here is thus mainly on the adequacy of the computational grid in capturing the SBLI flow physics. This was assessed by computing the SBLI-0.8-14 case (strongest shock, coldest wall;

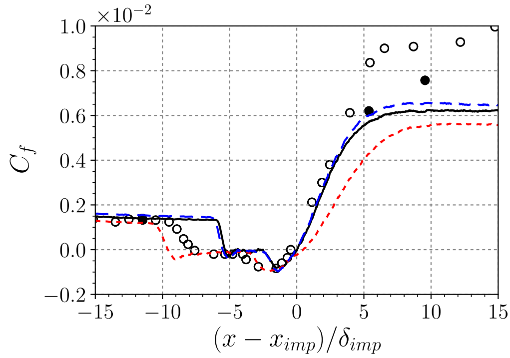

(a)Distribution of the mean skin friction coefficient

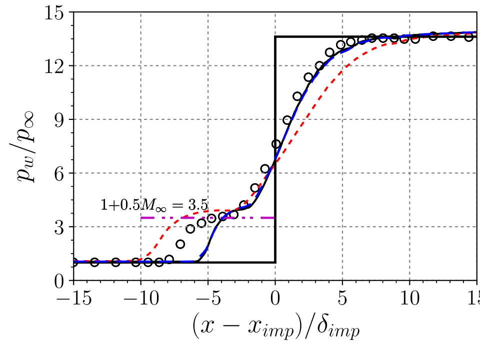

(b)Distribution of the mean wall pressure

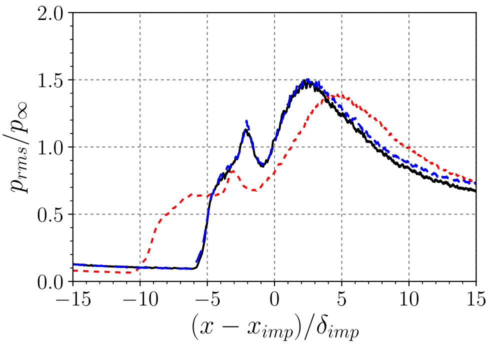

(c)Distribution of the root-mean-square wall pressure

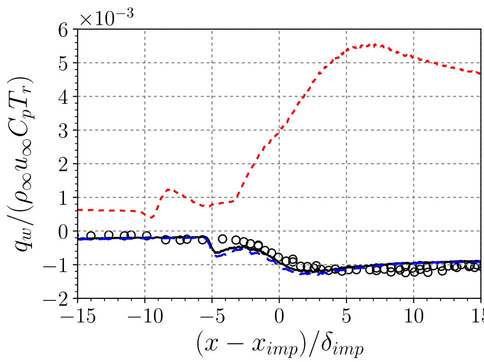

(d)Distribution of the mean wall heat flux

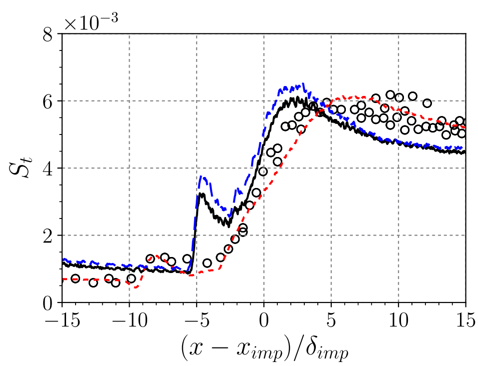

(e)Distribution of the mean Stanton number

FIG. 7. Mean flow properties across the interaction zone at $\varphi = 14^\circ$ flow deflection: cases SBLI-1.9-14 (dotted line), SBLI-0.8-14 (dashed line), and SBLI-0.8-14-H (solid line). The symbols indicate experimental measurements from Schülein [23]. In (a), the open circles are from oil film interferometry while the closed circles are from the measured velocity profile. The plateau pressure prediction according to Zukoski [41] is also shown in (b). (a) Distribution of the mean skin friction coefficient. (b) Distribution of the mean wall pressure. (c) Distribution of the root-mean-square wall pressure. (d) Distribution of the mean wall heat flux. (e) Distribution of the mean Stanton number.

thus, the most challenging in terms of resolution requirements) on a finer grid using both the base code developed at the University of Maryland and a different solver developed at the University of Rome. Both simulations used the same refined grid with $3400 \times 460 \times 280$ points, leading to a grid resolution of $\Delta x^+ = 4.7$, $\Delta y^+ = 0.5$, and $\Delta z^+ = 4.2$ in the incoming boundary layer. A similar setup was employed for both simulations, considering the same viscosity-temperature relationship (power law) and the digital filtering technique for the generation of the turbulent inflow. The two codes use different numerical methods, including different treatments of the viscous term (sixth-order finite difference vs finite-volume-like) and splitting of the convective term (Ducros *et al.* [28] vs Kennedy and Gruber [39]). The UMD code also employs a gentle sixth-order artificial dissipation which the Rome code does not.

The skin friction and Stanton number distributions are shown in Fig. 6 for all three cases. There is very little difference in the distributions between the three cases, verifying that the base grid is sufficiently fine. It is worth noting that the grid resolution requirements increase dramatically downstream of the interaction, the viscous length scale decreasing by a factor of $\approx$7. So, in a rigorous way, the simulations presented herein are true DNS only up to $(x - x_{\text{imp}})/\delta_{\text{imp}} \approx 4$, and large eddy simulations (LES) from that point on. This is nevertheless deemed sufficient for this study, due to the small differences between the results from the two different grids. We also emphasize that this study is focused on the interaction region, which shows very good agreement between the two grids. The same observation is valid when analyzing the Stanton number distribution.

It is worth noting that the spanwise domain size is about $3\delta_{\text{imp}}$ for all cases, while the size of the separation bubble varies up to $10\delta_{\text{imp}}$. Pasquariello *et al.* [40] performed a careful assessment of the influence of the domain width on the results for a strong SBLI with a separation bubble of size $15\delta_{\text{imp}}$ and found virtually unchanged results for domain width down to $2.25\delta_{\text{imp}}$. For this reason, the present domain width is believed to be sufficient.

C. Effect of wall temperature on the SBLI flow field

The spatial distribution of the mean skin friction coefficient C_f is shown in Fig. 7(a). The heated case separates first and reattaches practically in the same location as the cooled case. The agreement between numerical and wind-tunnel results is relatively good in the undisturbed boundary layer. In the interaction, curiously, it seems that the heated case compares better with the experiment at the beginning of the interaction. For $(x - x_{\text{imp}})/\delta_{\text{imp}} > 0$, the agreement is better for the cooled simulation. The skin friction distribution gradually relaxes to that of an equilibrium boundary layer, but in this region the experimental uncertainty is quite large. Note that the simulation at higher Reynolds number SBLI-0.8-14-H does not show a big discrepancy if compared to the one performed at lower Reynolds number. Thus, it appears that the impact of the shock strength or wall cooling is more important than the Reynolds number in determining the size of the interaction length scales.

The spatial distribution of the mean wall pressure p_w for the same cases, as well as the pressure jump predicted by the inviscid theory, are plotted in Fig. 7(b). Both simulations are typical of strong interactions, but the pressure plateau for the cooled case is smaller than the heated one. The final pressure is equal to the inviscid value in both cases. In Fig. 7(b) the plateau pressure prediction by Zukoski [41] is also plotted as reference.

It was found in supersonic SBLI that the peak root-mean-square wall pressure p_{rms} was stronger in cooled cases [18,19]. At $\text{Ma}_\infty = 2.28$, for example, the peak value for a case with wall conditions $T_w/T_r = 0.5$ was found to be $\sim$1.6 times higher than for a case with $T_w/T_r = 1.9$. Figure 7(c) shows that for the present configurations, the maximum values of the wall pressure fluctuation are practically the same in both situations. The wall-pressure fluctuations for simulations with $\varphi = 6^\circ$ (not shown) show only one local maximum, similar to the supersonic SBLI results from the previous study [19]. If the shock strength is very strong, it is possible to obtain two local peaks [40], as in SBLI-0.8-14. This is related to the shock foot location, specifically that the second reflected shock bifurcates (see Fig. 8), generating the middle peak. The mean turbulence kinetic energy $k = \widetilde{u_i'' u_i''}/2$

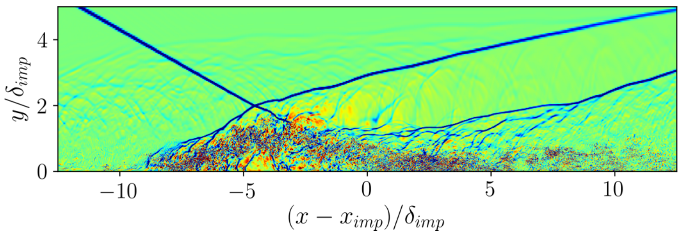

FIG. 8. Instantaneous dilatation field $\xi = \partial_j u_j$ for simulation with $T_w/T_r = 1.9$ and $\varphi = 14^\circ$ (case SBLI-1.9-14). Contour levels are shown in the range $-1 < \xi < 1$.

is amplified in the shear layer and also in the reflected shock location as clearly visualized in Fig. 9. Interestingly, the heated $\varphi = 14^\circ$ case (SBLI-1.9-14) shows a further qualitative change with an extended region of elevated $p_{\rm rms}$ between the point of separation and the first $p_{\rm rms}$ peak.

Figure 7(d) characterizes the heat transfer behavior across the interaction. Here, the heat transfer is normalized by $\rho_\infty u_\infty C_p T_r$ to allow a direct comparison between the heated and cooled cases. A strong amplification of the heat transfer rate is found in the interaction region with respect to the reference cooled or heated boundary layers, with a maximum increase of approximately a factor of 7 for the cooled wall and 9 for the heated wall. Note that these values are much higher than in the supersonic cases. The spatial distribution of the Stanton number is displayed in Fig. 7(e).

A useful correlation of heating variation with pressure for shock/turbulent boundary-layer interaction was found by Back and Cuffel [42]. They stated that the heat flux (or Stanton number) should scale as

$$\frac{q_{w,\max}}{q_{w,0}} = \left(\frac{p_{\max}}{p_\infty}\right)^n, \tag{4}$$

where $p_{\max}/p_\infty$ is the inviscid surface pressure ratio across the shock wave, $q_{w,0}$ is the wall heat flux value calculated in the incoming boundary layer, here taken at $x_0 = 21\delta_{\rm in}$. Back and Cuffel [42] and Holden [22] found $n = 0.85$ experimentally, while Hung and Barnett [43] obtained $n = 0.80$. Figure 10 shows the correlation of maximum heating with shock strength. Also plotted in the graphic are the laws that best describe the trend. While $n = 0.85$ describes precisely the trend for SBLI with a heated wall, for SBLI with cooled walls n is found to be relatively lower at the present conditions. We also note that the peak Stanton number occurs in the region where we found the largest uncertainties in the present results during the solution verification, and thus these results should be taken as approximate.

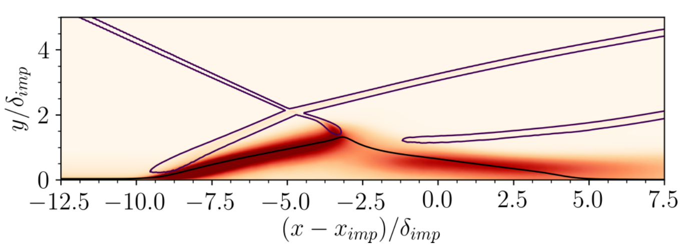

FIG. 9. Mean turbulence kinetic energy $k = \widetilde{u_i'' u_i''}/2$. Contour levels are shown in the range $0 < k/u_\infty^2 < 0.04$ with $T_w/T_r = 1.9$ and $\varphi = 14^\circ$ (case SBLI-1.9-14). The black line denotes the sonic line. Isocontour of the mean dilatation is shown in dark purple.

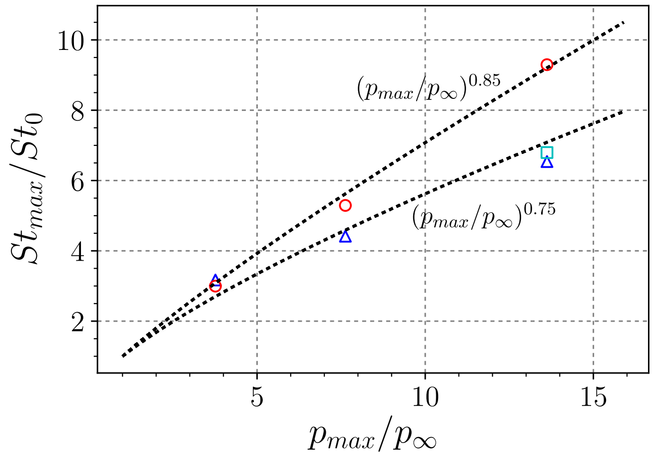

FIG. 10. Correlation of maximum heating with shock strength. Heated walls (red circles), cooled walls (blue triangles), and SBLI-0.8-14-H (green squares).

D. Pressure spectrum

The computation of temporal spectra requires long simulation times, which becomes particularly expensive under cooled wall conditions due to the increased resolution requirements. For this reason, only the spectrum for the heated case SBLI-1.9-14 was computed. The total simulation time was 1500 $\delta_{\text{in}}/u_\infty$.

The premultiplied wall pressure spectrum $f\,E(f)$ is displayed in Fig. 11 as a function of the Strouhal number $\text{Sr} = f\delta_0/u_\infty$ and the scaled coordinate $(x - x_{\text{imp}})/\delta_{\text{imp}}$. The spectrum is normalized, at each streamwise location, by the local value of the the root-mean-square quantity, in such a way that the integral over frequency is unity at each streamwise station. The premultiplied power spectral density (PSD) is obtained using Welch's method by splitting the signal in two segments with 50% overlapping which are individually Fourier transformed. Then, the frequency spectrum is obtained by averaging the periodograms of the various segments, minimizing the variance of the PSD estimator. Finally, the PSD is filtered by applying a Konno-Ohmachi smoothing [44] ensuring a constant bandwidth in a logarithmic scale.

The map of the wall pressure signal shows that part of the broadband energy in the premultiplied spectrum is found close to the foot of the first reflected shock, at $(x - x_{\text{imp}})/\delta_{\text{imp}} \approx -9$, at frequencies 2–3 orders of magnitude lower than the turbulent structures of the incoming boundary

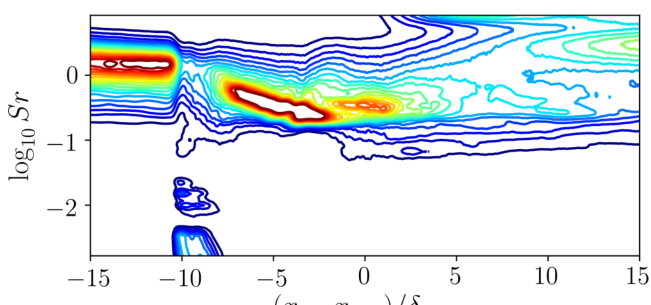

FIG. 11. Contours of premultiplied pressure spectrum $f\,E(f)$ for the SBLI-1.9-14 case with a heated wall. The spectrum is normalized in such a way that their integral over frequency is unity at each streamwise station.

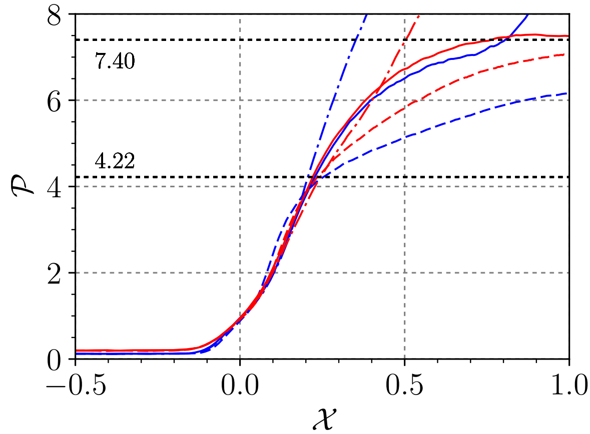

FIG. 12. Similarity function $\mathcal{P}$ [scaled pressure; Eq. (5)] plotted versus $\mathcal{X}$ [distance from separation point; Eq. (6)] evaluated for all SBLI cases. Cases: SBLI-0.8-06 (blue dashed line), SBLI-0.8-10 (blue dashed-dotted line), SBLI-0.8-14 (blue solid line), SBLI-1.9-06 (red dashed line), SBLI-1.9-10 (red dashed-dotted line), SBLI-1.9-14 (red solid line).

layer. Note that there is no low frequency oscillation related to the second reflected shock [for $(x - x_{\text{imp}})/\delta_{\text{imp}}$ from about 0 to 5, say; see Figs. 8 and 9]. Upstream of the interaction zone, the broadband energy in the premultiplied spectrum is typical of a canonical wall-bounded flow, with a peak at Sr ≈ 1 associated with the energetic turbulent structures of the boundary layer. Downstream of the interaction, the spectral density is broadened, and the peak is shifted to lower frequencies due to the thickening of the boundary layer.

E. Free interaction theory

Once a boundary layer separates, the flow field in the region near separation is dominated by the equilibrium interaction between the boundary layer and the external flow. Although the location of the point of separation is a function of the location and strength of the disturbance, the interacting flow upstream of the separation depends neither on the source of separation nor on the downstream geometry. This observation led Chapman *et al.* [45] to formulate the "free interaction" theory. A detailed description of the free interaction theory can be found in Refs. [46–50].

It can be shown that the nondimensional similarity variables within the free interaction zone are given by

$$\mathcal{P} = \frac{p - p_0}{q_0}\left[\frac{\left(M_0^2 - 1\right)^{1/2}}{2C_{f0}}\right]^{1/2}, \tag{5}$$

$$\mathcal{X} = \frac{x - x_{\text{sep}}}{\delta_0^*}\left[\left(M_0^2 - 1\right)^{1/2} C_{f0}\right]^{1/2}, \tag{6}$$

where $q_0 = 0.5\rho_0 u_0^2$. The subscript 0 indicates a reference point near beginning of separation interaction, taken as $x_0 = 21\delta_{\text{in}}$. The similarity function $\mathcal{P}(\mathcal{X})$ is plotted in Fig. 12.

It is remarkable how the initial pressure rise is almost identical among all present cases, including heated/cooled and different shock angles producing both weak and strong interactions. When comparing with other studies, however, the $\mathcal{P}(\mathcal{X})$ function does not appear to be universal. Defining $\mathcal{P}_s$ to be the value at the point of separation (i.e., at $\mathcal{X} = 0$), the present cases all have $\mathcal{P}_s \approx 1$. In contrast, Grossman and Bruce [51] found values ranging from 3.37 to 5.07, while Matheis and Hickel [52] found $\mathcal{P}_s = 1.6$ for regular and irregular SBLI at different deflection angles. In a much earlier study, Erdos and Pallone [46] proposed the specific value $\mathcal{P}_s = 4.22$ for turbulent flow (and

$\mathcal{P}_s = 0.81$ for laminar flow). Clearly, the free interaction scaled pressure at separation does not seem to have a universal value.

In what is presumably a coincidence, the Erdos and Pallone [46] value of $\mathcal{P}_s = 4.22$ instead corresponds very closely to where the similarity between the different cases breaks down in this study. Erdos and Pallone [46] also proposed that $\mathcal{P}_p$, the value at the pressure plateau, should be 6.0 in a turbulent flow and 1.47 in a laminar flow. Matheis and Hickel [52] found $\mathcal{P}_p = 7.4$ in their study, which agrees well with the present cases that display a strong interaction.

F. Interaction length scaling

The interaction length L_{int} is defined as the distance between the foot of the separation shock and the extrapolated wall impact point of the incident shock. In this study, the interaction length is well approximated by $L_{\text{int}} = x_{\text{imp}} - x_{\text{sep}}$. Note that the separation location has the same behavior as the interaction length and that the reattachment position remains constant for weak interactions and changes only for strong ones [19].

Using mass conservation properties along the interaction, Souverein *et al.* [27] carried out a scaling analysis, where the interaction length L_{int} was normalized by the displacement thickness of the incoming boundary layer δ_0^* and the function $g_3(\beta, \varphi) = \sin(\beta - \varphi)/[\sin(\beta)\sin(\varphi)]$ that takes into account the imposed flow deflection and the Mach number (φ and β are the deflection and shock angles, respectively). They then argued that this normalized interaction length should depend on a separation criterion defined as $\Delta P/\Delta P_{\text{sep}}$, where ΔP is the pressure jump across the interaction and ΔP_{sep} is the pressure jump required to make the boundary layer separate. The latter was estimated as $\Delta P_{\text{sep}} \approx q_0/k_1$, where q_0 is the dynamic pressure in the incoming boundary layer and k_1 is a coefficient for which they recommended the values of 3 for low Reynolds numbers ($\text{Re}_\theta \approx 5 \times 10^3$) and 2.5 for higher Reynolds numbers ($1 \times 10^4 < \text{Re}_\theta < 3 \times 10^5$). The interaction length scaled according to this scaling is shown in Fig. 13(a) together with a compilation of data found in the literature. This scaling works well for weak interactions but shows a larger spread between heated and cooled walls for stronger interactions.

Jaunet *et al.* [17] modified the scaling relationship through use of the free interaction theory by Chapman *et al.* [45] to better account for the effects of wall temperature. Specifically, they adjusted the estimation of the pressure jump required to make the boundary layer separate to $\Delta P'_{\text{sep}} = k_2 q_0 \sqrt{2C_{f0}/(M_0^2 - 1)^{1/2}}$, which now explicitly depends on the friction coefficient and the Mach number of the incoming boundary layer. They computed the value of the k_2 coefficient as $k_2 = 7.14$ based on an adiabatic case at $\text{Ma}_\infty = 2.28$, and validated the scaling on a range of cases at that Mach number but with different wall temperatures; this scaling was also found to be very accurate at the same $\text{Ma}_\infty = 2.28$ for heated/adiabatic/cooled walls and different Reynolds numbers in the DNS of Volpiani *et al.* [19].

The Jaunet *et al.* [17] scaling is validated for the present $\text{Ma}_\infty = 5$ in Fig. 13(b) together with the experimental data from [17]. The higher Mach number cases do not collapse on the lower Mach number ones. Adjusting the coefficient to $k_2 = 15$ produces a much better agreement across the Mach numbers, which shows that this coefficient is not a "constant"; it depends at least on the Mach number. We note that the dependence on the interaction strength (or separation criterion) agrees well after adjusting the k_2 coefficient, which shows that the Jaunet *et al.* [17] scaling does capture the correct dependence on ΔP and T_w/T_r.

VI. SUMMARY

In this paper, high-fidelity numerical simulations of an impinging shock interacting with a turbulent hypersonic boundary layer were performed and the effects of deviation angle and wall temperature on SBLI flow field were investigated. The flow conditions match the Schülein [23] experiments: free-stream Mach number $\text{Ma}_\infty = 5.0$, flow deflection angles of $\varphi = 6^\circ$, 10°, and 14° with wall-to-recovery temperature ratio of $T_w/T_r = 0.8$. Additional simulations were carried

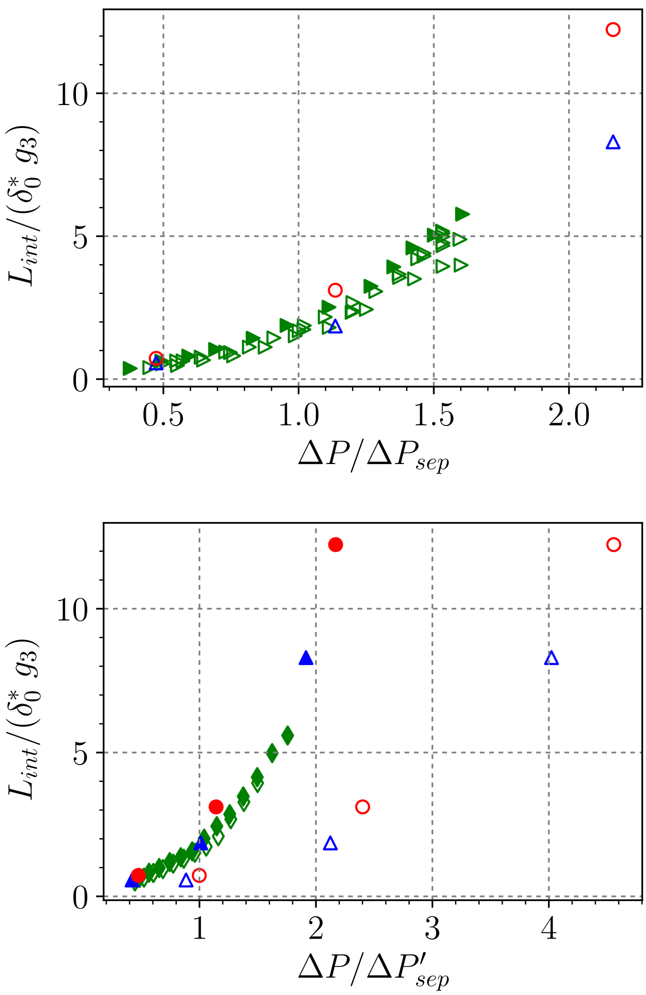

FIG. 13. Normalized interaction length L_{int} as a function of the separation criteria by Souverein *et al.* [27] (top) and Jaunet *et al.* [17] (bottom). Simulations with cooled (blue triangles) and heated (red circles) wall; open symbols scaled using the original constants ($k_1 = 3$ in the left figure, $k_2 = 7.14$ in the right), filled symbols scaled using the modified constant $k_2 = 15$. The compilation of results discussed in Souverein *et al.* [27] is also reported: adiabatic walls (open right triangle [3–5,53]) and heated walls (filled right triangle [54]). Experimental data from Jaunet *et al.* [17] at Mach ($\text{Ma}_\infty = 2.3$) and Reynolds ($\text{Re}_\theta = 5 \times 10^3$) numbers are also reported: adiabatic walls (open green diamond) and heated walls (filled green diamond).

out with a heated wall ($T_w/T_r = 1.9$) to investigate the impact of the wall thermal condition on shock/boundary-layer interactions in the hypersonic regime. It was shown that numerical results do not match the experimental data, and it was argued that the most plausible cause of this discrepancy is the presence of 3D effects in the experiment. Since experimental and numerical studies are used to validate Reynolds-averaged Navier-Stokes (RANS) models, we highlight the importance of both analyses to be carried out in parallel. We believe that simulations can provide more controlled results, due to the possibility of validation with numerous boundary-layer data available in the literature, as done in this study. It is observed that wall cooling decreases the interaction scales and size of the separation bubbles in agreement with previous studies. The impact of the wall thermal condition on the wall pressure fluctuations is less pronounced than in supersonic SBLI, where wall cooling increases p_{rms}. We show that the free interaction theory remains valid in the hypersonic regime even at different wall thermal conditions. The similarity scaling of the interaction length remains an open problem. The scaling by Souverein *et al.* [27] captures the effects of the shock strength and the Mach number but misses the effect of the wall thermal condition, while the scaling by Jaunet *et al.* [17] captures the effects of the shock strength and the wall thermal condition but misses the effect of the Mach number.

ACKNOWLEDGMENTS

The authors would like to thank Dr. E. Schülein for fruitful discussions and for sharing the experimental data. P.S.V. and J.L. were supported by the Air Force Office of Scientific Research (Grant No. FA9550-16-1-0385). M.B. was supported by the Scientific Independence of young Researchers program 2014 (Active Control of Shock-wave Boundary-layer Interaction project, Grant No. RBSI14TKWU), funded by MIUR. The work was performed using HPC resources of the University of Maryland (DeepThought2), the Maryland Advanced Research Computing Center (MARCC), and the Argonne Leadership Computing Facility, which is a DOE Office of Science User Facility supported under Contract No. DE-AC02-06CH11357.

[1] G. S. Settles, S. M. Bogdonoff, and I. E. Vas, Incipient separation of a supersonic turbulent boundary layer at high reynolds numbers, AIAA J. **14**, 50 (1976).

[2] F. O. Thomas, C. M. Putnam, and H. C. Chu, On the mechanism of unsteady shock oscillation in shock wave/turbulent boundary layer interactions, Exp. Fluids **18**, 69 (1994).

[3] P. Dupont, C. Haddad, and J. F. Debieve, Space and time organization in a shock-induced separated boundary layer, J. Fluid Mech. **559**, 255 (2006).

[4] S. Piponniau, J. P. Dussauge, J. F. Debieve, and P. Dupont, A simple model for low-frequency unsteadiness in shock-induced separation, J. Fluid Mech. **629**, 87 (2009).

[5] L. J. Souverein, P. Dupont, J.-F. Debiève, B. W. Van Oudheusden, and F. Scarano, Effect of interaction strength on unsteadiness in shock-wave-induced separations, AIAA J. **48**, 1480 (2010).

[6] N. A. Adams, Direct simulation of the turbulent boundary layer along a compression ramp at M= 3 and $\mathrm{Re}_\theta = 1685$, J. Fluid Mech. **420**, 47 (2000).

[7] D. P. Rizzetta, M. R. Visbal, and D. V. Gaitonde, Large-eddy simulation of supersonic compression-ramp flow by high-order method, AIAA J. **39**, 2283 (2001).

[8] M. Wu and M. P. Martin, Analysis of shock motion in shockwave and turbulent boundary layer interaction using direct numerical simulation data, J. Fluid Mech. **594**, 71 (2008).

[9] S. Priebe, M. Wu, and M. P. Martin, Direct numerical simulation of a reflected-shock-wave/turbulent-boundary-layer interaction, AIAA J. **47**, 1173 (2009).

[10] E. Touber and N. D. Sandham, Large-eddy simulation of low-frequency unsteadiness in a turbulent shock-induced separation bubble, Theor. Comput. Fluid Dyn. **23**, 79 (2009).

[11] S. Pirozzoli and M. Bernardini, Direct numerical simulation database for impinging shock wave/turbulent boundary-layer interaction, AIAA J. **49**, 1307 (2011).

[12] G. Aubard, X. Gloerfelt, and J.-C. Robinet, Large-eddy simulation of broadband unsteadiness in a shock/boundary-layer interaction, AIAA J. **51**, 2395 (2013).

[13] J. W. Nichols, J. Larsson, M. Bernardini, and S. Pirozzoli, Stability and modal analysis of shock/boundary layer interactions, Theor. Comput. Fluid Dyn. **31**, 33 (2017).

[14] M. Hayashi, A. Sakurai, and S. Aso, Measurement of heat-transfer coefficients in shock wave-turbulent boundary layer interaction regions with a multi-layered thin film heat transfer gauge, NASA Tech. Memo. TM-77958, p. 455, 1986.

[15] F. W. Spaid and J. C. Frishett, Incipient separation of a supersonic, turbulent boundary layer, including effects of heat transfer, AIAA J. **10**, 915 (1972).

[16] L. H. Back and R. F. Cuffel, Shock wave/turbulent boundary-layer interactions with and without surface cooling, AIAA J. **14**, 526 (1976).
[17] V. Jaunet, J. F. Debiève, and P. Dupont, Length scales and time scales of a heated shock-wave/boundary-layer interaction, AIAA J. **52**, 2524 (2014).
[18] M. Bernardini, I. Asproulias, J. Larsson, S. Pirozzoli, and F. Grasso, Heat transfer and wall temperature effects in shock wave turbulent boundary layer interactions, Phys. Rev. Fluids **1**, 084403 (2016).
[19] P. S. Volpiani, M. Bernardini, and J. Larsson, Effects of a nonadiabatic wall on supersonic shock/boundary-layer interactions, Phys. Rev. Fluids **3**, 083401 (2018).
[20] G. S. Settles and L. J. Dodson, Supersonic and hypersonic shock/boundary-layer interaction database, AIAA J. **32**, 1377 (1994).
[21] G. M. Elfstrom, Turbulent hypersonic flow at a wedge-compression corner, J. Fluid Mech. **53**, 113 (1972).
[22] M. Holden, Shock wave-turbulent boundary layer interaction in hypersonic flow, in *15th Aerospace Sciences Meeting* (AIAA, Reston, VA, 1977), p. 45.
[23] E. Schülein, Skin friction and heat flux measurements in shock/boundary layer interaction flows, AIAA J. **44**, 1732 (2006).
[24] E. Schülein, P. Krogmann, and E. Stanewsky, Documentation of two-dimensional impinging shock/turbulent boundary layer interaction flows, DLR, German Aerospace Research Center, Paper 1 B 223-96 A 49, Oct. 1996.
[25] N. D. Sandham, E. Schülein, A. Wagner, S. Willems, and J. Steelant, Transitional shock-wave/boundary-layer interactions in hypersonic flow, J. Fluid Mech. **752**, 349 (2014).
[26] A. Wagner, J. M. Schramm, K. Hannemann, R. Whitside, and J.-P. Hickey, Hypersonic shock wave boundary layer interaction studies on a flat plate at elevated surface temperature, in *International Conference on RailNewcastle Talks* (Springer, Berlin, 2017), pp. 231–243.
[27] L. J. Souverein, P. G. Bakker, and P. Dupont, A scaling analysis for turbulent shock-wave/boundary-layer interactions, J. Fluid Mech. **714**, 505 (2013).
[28] F. Ducros, F. Laporte, T. Souleres, V. Guinot, P. Moinat, and B. Caruelle, High-order fluxes for conservative skew-symmetric-like schemes in structured meshes: application to compressible flows, J. Comput. Phys. **161**, 114 (2000).
[29] E. Johnsen, J. Larsson, A. V. Bhagatwala, W. H. Cabot, P. Moin, B. J. Olson, P. S. Rawat, S. K. Shankar, B. Sjögreen, H. C. Yee *et al.*, Assessment of high-resolution methods for numerical simulations of compressible turbulence with shock waves, J. Comput. Phys. **229**, 1213 (2010).
[30] M. Klein, A. Sadiki, and J. Janicka, A digital filter based generation of inflow data for spatially developing direct numerical or large eddy simulations, J. Comput. Phys. **186**, 652 (2003).
[31] M. P. Simens, J. Jiménez, S. Hoyas, and Y. Mizuno, A high-resolution code for turbulent boundary layers, J. Comput. Phys. **228**, 4218 (2009).
[32] J. Jiménez Sendín, S. Hoyas, M. P. Simens, and Y. Mizuno, Turbulent boundary layers and channels at moderate reynolds numbers, J. Fluid Mech. **657**, 335 (2010).
[33] A. J. Smits and J.-P. Dussauge, *Turbulent Shear Layers in Supersonic Flow* (Springer, New York, 2006).
[34] A. Trettel and J. Larsson, Mean velocity scaling for compressible wall turbulence with heat transfer, Phys. Fluids **28**, 026102 (2016).
[35] P. Schlatter and R. Örlü, Assessment of direct numerical simulation data of turbulent boundary layers, J. Fluid Mech. **659**, 116 (2010).
[36] P. S. Volpiani, P. S. Iyer, S. Pirozzoli, and J. Larsson, Towards the universality of the mean velocity profile for compressible turbulent boundary layers (unpublished).
[37] J. Délery and J.-P. Dussauge, Some physical aspects of shock wave/boundary layer interactions, Shock Waves **19**, 453 (2009).
[38] P. J. K. Bruce, D. M. F. Burton, N. A. Titchener, and H. Babinsky, Corner effect and separation in transonic channel flows, J. Fluid Mech. **679**, 247 (2011).
[39] C. A. Kennedy and A. Gruber, Reduced aliasing formulations of the convective terms within the navier–stokes equations for a compressible fluid, J. Comput. Phys. **227**, 1676 (2008).
[40] V. Pasquariello, S. Hickel, and N. A. Adams, Unsteady effects of strong shock-wave/boundary-layer interaction at high reynolds number, J. Fluid Mech. **823**, 617 (2017).

[41] E. E. Zukoski, Turbulent boundary-layer separation in front of a forward-facing step, AIAA J. **5**, 1746 (1967).

[42] L. H. Back and R. F. Cuffel, Changes in heat transfer from turbulent boundary layers interacting with shock waves and expansion waves, AIAA J. **8**, 1871 (1970).

[43] F. Hung and D. Barnett, Shockwave-boundary layer interference heating analysis, in *11th Aerospace Sciences Meeting* (AIAA, Reston, VA, 1973), p. 237.

[44] K. Konno and T. Ohmachi, Ground-motion characteristics estimated from spectral ratio between horizontal and vertical components of microtremor, Bull. Seismol. Soc. Am. **88**, 228 (1998).

[45] D. R. Chapman, D. M. Kuehn, and H. K. Larson, Investigation of separated flows in supersonic and subsonic streams with emphasis on the effect of transition, NACA Rept. 1356, 1957.

[46] J. Erdos and A. Pallone, Shock-boundary layer interaction and flow separation, in *Proceedings of the Heat Transfer and Fluid Mechanics Institute* (Stanford University Press, Stanford, CA, 1962).

[47] P. Carrière, M. Sirieix, and J.-L. Solignac, Similarity properties of the laminar or turbulent separation phenomena in a non-uniform supersonic flow, *Applied Mechanics* (Springer, New York, 1969), pp. 145–157.

[48] A. F. Charwat, Supersonic flows with imbedded separated regions, *Advances in Heat Transfer*, Vol. 6 (Elsevier, Amsterdam, 1970), pp. 1–132.

[49] J. Délery and J. G. Marvin, Shock-wave boundary layer interactions, Tech. Rep. AGARDograph 280. AGARD, Neuilly Sur Seine, France, 1986.

[50] H. Babinsky and J. K. Harvey, *Shock Wave-Boundary-Layer Interactions*, Vol. 32 (Cambridge University Press, Cambridge, 2011).

[51] I. J. Grossman and P. J. K. Bruce, Confinement effects on regular–irregular transition in shock-wave–boundary-layer interactions, J. Fluid Mech. **853**, 171 (2018).

[52] J. Matheis and S. Hickel, On the transition between regular and irregular shock patterns of shock-wave/boundary-layer interactions, J. Fluid Mech. **776**, 200 (2015).

[53] L. J. Souverein, B. W. Van Oudheusden, F. Scarano, and P. Dupont, Application of a dual-plane particle image velocimetry (dual-piv) technique for the unsteadiness characterization of a shock wave turbulent boundary layer interaction, Meas. Sci. Technol. **20**, 074003 (2009).

[54] H. Laurent, Turbulence d'une interaction onde de choc/ couche limite sur une paroi plane adiabatique ou chauffée, Ph.D. thesis, Université d'Aix-Marseille II, Marseille, France, 1996.